Check for updates

Miniaturized optical fiber probe for prostate cancer screening

ANTONIO IELE,[1] **ARMANDO RICCIARDI,**[1,4] (iD) **CLAUDIA PECORELLA,**[2] **ANDREA CIRILLO,**[2] **FANNY FICUCIELLO,**[2] **BRUNO SICILIANO,**[2] **ROBERTO LA ROCCA,**[3] **VINCENZO MIRONE,**[3] **MARCO CONSALES,**[1] **AND ANDREA CUSANO**[1]

[1]*Optoelectronics Group, Engineering Department, University of Sannio, Benevento, I-82100, Italy*
[2]*PRISMA Lab, Department of Electrical Engineering and Information Technology, University of Naples Federico II, Naples, I-80125, Italy*
[3]*Department of Neurosciences, Sciences of Reproduction and Odontostomatology, Urology Unit, University of Naples Federico II, Naples, I-80125, Italy*
[4]*aricciardi@unisannio.it*

Abstract: Tissue elasticity is universally recognized as a diagnostic and prognostic biomarker for prostate cancer. As the first diagnostic test, the digital rectal examination is used since malignancy changes the prostate morphology and affects its mechanical properties. Currently, this examination is performed manually by the physician, with an unsatisfactory positive predictive value of 42%. A more objective and spatially selective technique is expected to provide a better prediction degree and understanding of the disease. To this aim, here we propose a miniaturized probe, based on optical fiber sensor technology, for mechanical characterization of the prostate with sub-millimeter resolution. Specifically, the optical system incorporates a customized Fiber Bragg Grating, judiciously integrated in a metallic cannula and moved by a robotic arm. The probe enables the local measurement of the force upon tissue indentation with a resolution of 0.97 mN. The system has been developed in such a way to be potentially used directly *in vivo*. Measurements performed on phantom tissues mimicking different stages of the prostatic carcinoma demonstrated the capability of our device to distinguish healthy from diseased zones of the prostate. The study on phantoms has been complemented with preliminary *ex vivo* experiments on real organs obtained from radical surgeries. Our findings lay the foundation for the development of advanced optical probes that, when integrated inside biopsy needle, are able to perform *in vivo* direct mechanical measurements with high sensitivity and spatial resolution, opening to new scenarios for early diagnosis and enhanced diagnostic accuracy of prostate cancer.

1. Introduction

Prostate cancer is the 3rd most common cause of cancer death, and the first common cause of cancer in men [1] The digital rectal examination (DRE) of the prostate, together with prostate specific antigen (PSA), is the primary screening test for patients, and it is used to detect hard areas of decreased elasticity (tumor) from healthy soft tissue [2]. However, DRE is highly subjective and the results strongly depend on the skill and experience of the physicians [3]. In addition, DRE may only have higher levels of accuracy when prostate cancer is at a more advanced stage, which limits its utility as a tool for early stage disease detection. Consequently, DRE specificity is only 40%, and neither a positive nor a negative DRE test result is sufficient to enable a conclusive diagnosis without further evaluation [4]. Improving upon the DRE's inaccuracies and providing new tools for mechanical characterization is of key importance to assess, monitor and understand the prostate cancer disease.

Current research efforts into the use of elasticity as a biomarker for prostate cancer have focused on two major groups of assessment: indirect characterization techniques are based on the monitoring for changes to the images, taken either by ultrasound and magnetic resonance, while direct testing involves applying a force directly on the tissue and recording the resulting deformation [1]. There is also considerable potential in combining information from direct and indirect techniques. Multiple studies showing improvements in disease detection by combining structural imaging with elasticity characterization have been reported [5–7].

So far, experimental studies dealing with direct mechanical measurements of the prostate tissue were based on the use of conventional force sensor technologies such as load cells [8–11], piezo-resistive [12] and resonance sensors [13,14]. Although these systems have been successfully tested on *ex vivo* experiments, the dimension of the force sensors used, typically of several millimeters, may prevent their practical use in *in vivo* applications. Consequently, there is a growing interest in developing miniaturized probes able to perform mechanical measurements directly *in vivo*, to be eventually used in combination with standard screening procedures such as the transrectal biopsy.

In this scenario, optical fiber sensors look particularly advantageous due to their inherent properties such as compact size, biocompatibility, non-toxicity, chemical inertness and electro-magnetically inert nature [15–17]. In the particular case of tissue mechanical characterization applications, optical fiber sensors based on both Fabry-Perot interferometers [18,19] and Fiber Bragg Gratings (FBGs) [20–24] have been proposed.

Specifically, FBGs have been used as force sensor for minimally invasive surgery [20,24], for the detection of tissue abnormalities during the surgery operations [22] and for biomechanical testing of cartilage tissues [24]. FBGs have been also mounted on the Da Vinci surgical arm for force measurement during surgical tasks [21]. Force resolutions typically range from 0.93mN [22] to 2.5mN [20], depending on the complexity of the sensor packaging. An optical dynamic instrumented palpation sensor has been recently reported for the specific case of prostate cancer screening [18]. The optical fiber probe is made of a dynamically actuated membrane sensor based on a Fabry–Pérot interferometer. The experimental tests were performed on a prostate phantom. In all the above mentioned systems, the optical fiber sensors are integrated in quite complex mechanical packaging that enhances the sensitivity at the expenses of the overall size.

In this framework, here we propose a miniaturized sensor based on optical fiber technology able to measure the tissue elasticity with sub-millimeter resolution. Specifically, the system incorporates a customized FBG suitably integrated inside a metallic cannula used for clinical applications and moved by a robotic arm. The developed sensor is an evolution of a smart needle developed for a different clinical case of interest that is the epidural space identification [25–27]. In this regard, it is interesting to remark that the same technology can be successfully applied to different clinical scenarios in line with the lab-on-needle vision. Although several systems based on optical fiber sensors have been already used for mechanical properties of biological tissues [18–24], our device exhibits unique features such as the lightweight, the miniaturization and the sub-millimeter spatial resolution. In fact, our configuration does not require the use of a sophisticated packaging system, and it has been developed to be potentially integrated in standard transrectal biopsy needles currently used in clinical practice.

The functionality of the developed sensor has been assessed by means of different tests carried out on silicone membranes and phantom tissues mimicking different stages of the prostatic carcinoma. Finally, we also provide preliminary results concerning *ex vivo* experiments on real organs obtained from radical surgeries. The measured elasticity coefficients are in line with those reported in previous studies. Overall, our device may open new possibilities for early diagnosis and enhanced diagnostic accuracy of prostate cancer.

2.   Methods

2.1.   Force sensor

The system used in this work is shown in Fig. 1(a); it essentially consists of an optical fiber probe inserted inside the lumen of an 18-gauge metallic cannula and locked to it in such a way that the tip comes out by 2 mm. In this configuration, the optical probe is in direct contact with the membrane to be analyzed during the indentation procedure.
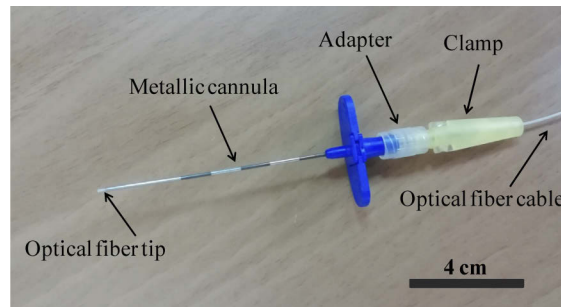

Fig. 1. Picture the developed system.

Specifically, the optical probe is made of an FBG written in an 80 μm fiber by means of the draw-tower process [28]. The FBG is coated by a Hytrel layer with an overall diameter of 0.9 mm that perfectly matches the internal lumen size of the cannula. Thin layers of Ormocer and Silicone are used as buffer layers to improve the adhesion between silica glass and Hytrel.

Basically, The FBG is a fiber section (8mm long in our case) characterized by a refractive index periodic modulation of its core [29]. The FBG is a narrow-band reflection filter for a specific wavelength given by the well-known relation, i.e. $\lambda_B = 2\,n_{eff}\Lambda$, where n_{eff} is effective refractive index of the fiber, and Λ is the modulation pitch. The Bragg wavelength λ_B shifts towards shorter/longer wavelengths when a compression/expansion of the grating pitch Λ occurs. The ratio between fiber and the Hytrel coating radius is chosen to enhance the force sensitivity of the optical probe, which is the Bragg wavelength shift in response to the pressure applied on its tip [25]. By exploiting this simple transduction mechanism, it is possible to use the FBG as a force sensor. In fact, the optical probe is locked to the cannula with a clamp-style connector that firmly holds in position the probe, so that it can be compressed while protected by the cannula. A standard luer lock adapter guarantees the connection of the clamp-style connector to the metallic cannula.

2.2.   Interrogation unit

A commercial interrogation unit (Hyperion Optical Sensing Instrument si155) was used to measure the Bragg wavelength shift as a function of time during indentation experiments [30]. The interrogation system is a compact console characterized by a wavelength operating range from 1500 to 1580 nm, and a scan frequency up to 5 kHz. The wavelength stability and accuracy are 1 pm for a scan frequency of 1 kHz used in our experiments. An Ethernet port and a user-friendly interface allows to control the instrument by using a PC.

2.3.   Sensor calibration

A calibration procedure was implemented to find the relationship between the optical probe wavelength shift and the force applied on its tip. To this aim, the probe was mounted on a metallic stage driven by a DC motor, used to control the movements along the (vertical) z axis. The compression on the fiber tip was impressed by pushing it onto the rigid (and non-deformable)

plane of a digital balance (nominal resolution 0.1 grams). The distance between the sensor and the balance was further controlled by means of a laser distance meter. The Bragg wavelength shift was measured as a function of different loads. The results are shown in Fig. 2(b), where the load is expressed in Newton.
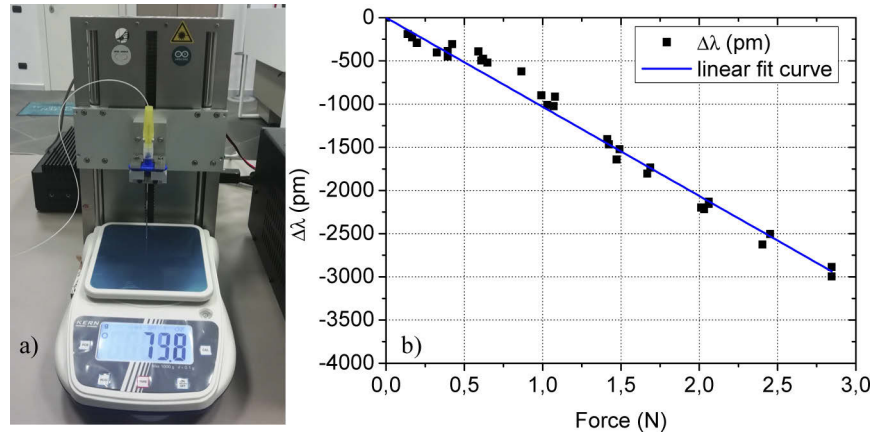

Fig. 2. Calibration setup (a) and Force calibration curve of the developed probe (b).

The calibration curve exhibits a pretty linear trend with an R-squared coefficient larger than 0.99. The probe sensitivity ($\Delta\lambda/\Delta N$) is 1031 pm/N, that is about 2 times higher than that obtained in our previous work (553 pm/N) [26] The sensitivity enhancement is due to the reduction of the fiber diameter from 125 to 80 micron [25]. The sensor resolution is estimated to be 0.97 mN that is the ratio between the sensitivity (1031 pm/N) and the interrogator resolution (1 pm). This resolution is very similar to the values obtained in more complex configurations exploiting FBGs, in which values of 2.55 mN [20] and 0.93 mN were demonstrated.

2.4. Experimental methodology: indentation tests

2.4.1. Experiments on silicone membranes and phantom tissue

The indentation tests over silicone membranes and phantom tissue were performed by moving the optical probe with a robotic arm (KUKA LBR Med 7) in order to accurately control the indentation depth. A customized holder for installing the optical probe on the robot end effector was realized by means of a 3D printing system (see Fig. 3).

The same robotic arm was used to perform indentation experiments on different prostate phantom tissues mimicking different stages of the prostate cancer. The phantoms are provided by 3B Scientific and they are developed for practicing procedures (details in the results and discussion section). During the indentation tests, the prostate models were suitably blocked in position by using a 3D printed holder. The phantom tissues were indented over more than 20 points separated by 5 mm one from each other. The indentation speed was 2 mm/s. The indentation and relaxation (i.e. the time interval between two consecutive indentations) duration was set to 6 seconds. The indentation depths were determined starting from a zero-value that was manually pre-set before performing the tests. In other words, each model was pre-scanned (before the indentation) with the robot, exploiting a manual guidance-based approach, to find the right coordinates parameters along the three axes of the contact point between the probe and the tissue. This step was performed manually and the contact was determined by considering the point for which a Bragg wavelength shift of 40 pm was measured. This procedure was made possible by the fact that each phantom is deterministic and all the contact points are fixed once that the gland has been suitably positioned with respect to a reference point.
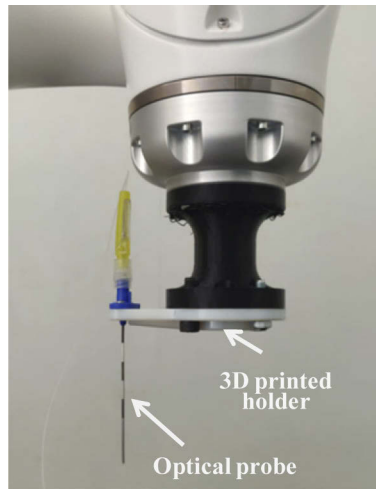
Fig. 3. Optical fiber probe installed on the robotic arm for the indentation experiments.

2.4.2. Ex vivo experiments

In the case of *ex vivo* measurements, the strong non-uniformity of the surface and the variable dimensions of the glands do not allow to pre-determine the contact point. In order to circumvent this problem a force control algorithm was implemented. The force control algorithm, also referred to as admittance control, allows to automatically detect a contact between the probe and the prostate under analysis. Starting from a points' map, generated on a virtual x-y plane collocated some centimetres under the prostate, through admittance control the robot end effector, and thus the probe, gets closer to the prostate until a contact is detected. Once in contact, the robot stops itself and sets the reached position as the starting point for the indentation analysis. Admittance control strategy controls the robot dynamics according to the following equation:

$M\ddot{x}_d + D\dot{x}_d = f_d - f_m$, where $f_d \in \mathcal{R}^3$ is the desired force the robot shall exert on the contact point located on the prostate, $f_m \in \mathcal{R}^3$ is the force measured with the probe, $M, D \in \mathcal{R}^{3x3}$ are positive defined matrix that influence the robot motion dynamics, $\ddot{x}_d, \dot{x}_d \in \mathcal{R}^3$ are the acceleration and the velocity of the robot end effector, respectively. In the specific case $f_d = [0, 0, f_{dz}]$ with $f_{dz} = 0.05$ N.

For further details on the force control algorithm, the reader can refer to [31]. The map of points that defines the starting points for the admittance control is automatically generated through a SW tool. The latter requires as input 4 points, preliminary and manually acquired. The 4 points are the vertexes of a quadrilateral representing the perimeter of the prostate area under analysis.

The indentation depth was set to 2 mm for all the points, while the indentation speed was 0.2mm/s. With respect to the experiments on the phantom, the indentation speed is 10 times lower in order to preserve the mechanical properties of the prostate tissue. This is because the prostate has to be further analyzed according to the standard pathologist procedure. Following the standard of the 12-core transrectal ultrasound-guided prostate needle biopsy, each prostate was indented on 12 different points pertaining to 12 different areas (4 on the Base, 4 in the Midgland and 2 on the Apex zone).

3. Results and discussion

3.1. Tests on silicone membranes

First, in order to assess the working principle of our device, we carried out some preliminary indentation tests of silicone membranes typically used in clinical tests to mimic the consistencies of biological tissues. In particular, we used silicone membranes provided by Smooth-On (diameter of 5 cm and thickness of 6 mm) with different values of hardness, and specifically 00–50 (Shore 00 type Hardness Scale), 10A and 30A (Shore A type Hardness Scale). The hardness nominal values of the membranes are taken from the material datasheet. Although hardness and elasticity are not the same, they are strongly related between each other, since the hardness (H) of a material tends to increase with an increase in its elastic modulus (E) [32]. In the specific case of silicones, the correlations between H and E are created empirically and suffer from significant scatter in different data sets available [33].

Figure 4(a) shows the Bragg wavelength as a function of time measured during repeated indentations in the same point of the silicone membrane (10 shore hardness type A) with a depth of 3 mm. A zoomed in image of the last indentation test is shown in Fig. 4(b). Indentation speed was set to 2 mm/s. Once that the final indentation depth was achieved, the probe was maintained in a fixed position for 6 seconds; successively, it was released and a new indentation was performed after 10 seconds. This procedure was studied and optimized in order to achieve a stable steady state condition when the probe is fully compressed and relaxed. The overall wavelength shift was evaluated as the difference between the steady states, highlighted by magenta and green stars in the plot. The repeatability analysis demonstrates that the probe has an accuracy of 0.4%, evaluated as the ratio between the average wavelength shift (902 pm) and its standard deviation (3.5 pm).
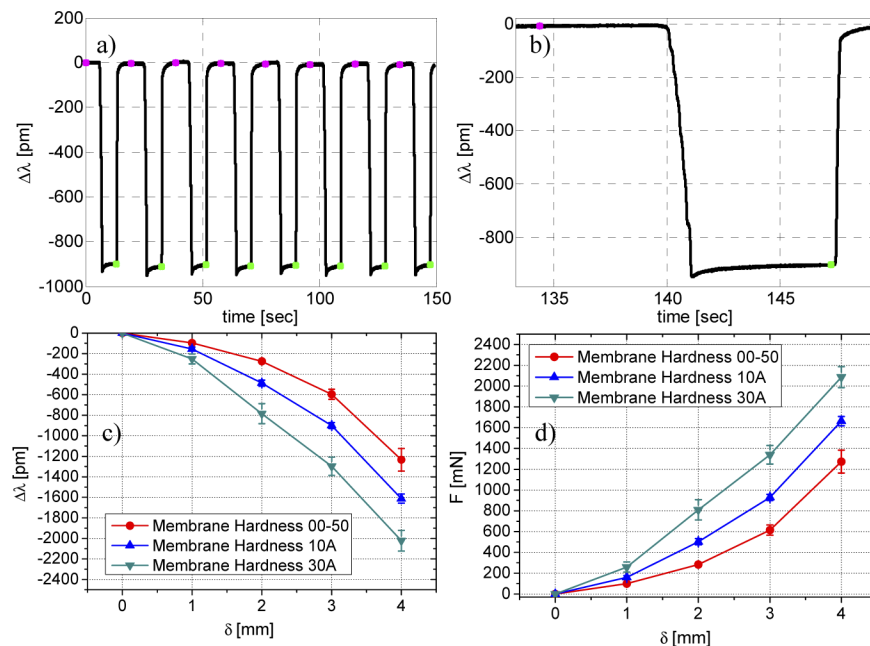

Fig. 4. (a) FGB response (Bragg wavelength shift) measured during the repeatability test. (b). zoomed in image of (a) Wavelength shift (c) and Force (d) as a function of the indentation depth for the three analyzed silicone membranes.

Successively, we performed indentation experiments on silicone membranes with different hardness. Each membrane was indented in the same point, at different depths, namely, 1, 2, 3 and 4 mm. The results are shown in Fig. 4(c), where the error bars represent the standard deviations calculated over 10 measurements. As expected, the wavelength shift has a decreasing trend as a function of the indentation depth. As the indentation depth increases, the probe, and thus the FBG, undergoes a larger compression inducing a blue-shift of the Bragg wavelength. Moreover, larger negative wavelength shifts are measured for harder membranes. In fact, the larger is the membrane hardness, the larger is the compression which undergoes the probe at the same indentation depth. By exploiting the wavelength-to-force conversion factor measured during the calibration procedure (i.e. 1.03 nm/N), it is possible to calculate the force F exerted on the probe tip during different indentations, as shown in Fig. 4(d). The larger is the indentation depth, the larger is the difference among the measured Force values over the different membranes. In principle, these curves could be fitted by exploiting the relationship between the force F and the indentation depth δ [34]:

$$F = \frac{(g \cdot E \cdot \delta^n)}{(1 - \nu^2)}, \tag{1}$$

where g and n are coefficients that depends on the geometry of tip of the (rigid) indenter, while E and ν are the Young modulus and the Poisson coefficient of the membrane, respectively. However, in our case, determining the values of g and n is not trivial since the indenter is not uniform being formed by two concentric cylinders made of glass (i.e. the fiber itself in which the FBG is written) and the external Hytrel coating. Moreover, it is important to underline that the above relationship is valid only for indentation depth smaller than 10% of the total membrane thicknesses that is not our case [35].

3.2. *Tests on phantom tissue*

Indentation experiments were also carried out on three different models of prostate tissues (shown in Fig. 5) provided by 3B Scientific. More specifically, the prostate 1 mimics a benign but slightly enlarged prostate (Fig. 5(a)), the prostate 2 simulates an early stage of carcinoma in which a single compact nodule is palpable in the right upper quadrant (red circle in Fig. 5(b)); prostate 3 mimics a carcinoma characterized by a lump that has enlarged and developed a compact external mass on the surface of the prostate (Fig. 5(c)). Unfortunately, we do not have any kind of information about the mechanical properties of the prostate phantoms.

Each prostate model was divided in three lines corresponding to three zones in which the prostate is technically divided (apex, midgland and base). Seven indentation points were chosen for each line according to the points sequence shown in Fig. 5. Some indentation points were added in the case of prostate 2 and 3. The indentation depth was 3 mm for all the points except for the points corresponding to the hard and visible carcinoma (points #5, 6, 8, 9 in Fig. 5(c)) that were indented with a depth of 1mm in order to avoid the sensor damage. Each test was repeated 3 times so that the error bars shown in Fig. 5(g)-(i) represent the standard deviation over 3 measurements.

Figure 5(d), Fig. 5(e) and Fig. 5(f) show the sensorgrams (i.e. the wavelength shifts as a function of time) pertaining to the indentation experiments. In the same figure, we also report the measured force normalized with respect to the relative indentation depth.

In the case of (healthy) prostate 1, the ratio F/δ value is quite constant over all the analyzed indentation points. The average and standard deviation are 0.21 N/mm and 0.016 N/mm, respectively. The points relative to base right lateral and medial exhibit slightly larger values but all below 0.25 N/mm, which corresponds to the maximum value registered for the 21 indentation points. In the case of prostate 2, the ratio F/δ is quite constant (average and std dev are 0.2 N/mm and 0.080 N/mm respectively) except for point # 13 for which the ratio $F/\delta = 0.56$ [N/mm]. This point is a clear indication of a diseased zone of the prostate. This trend is more evident
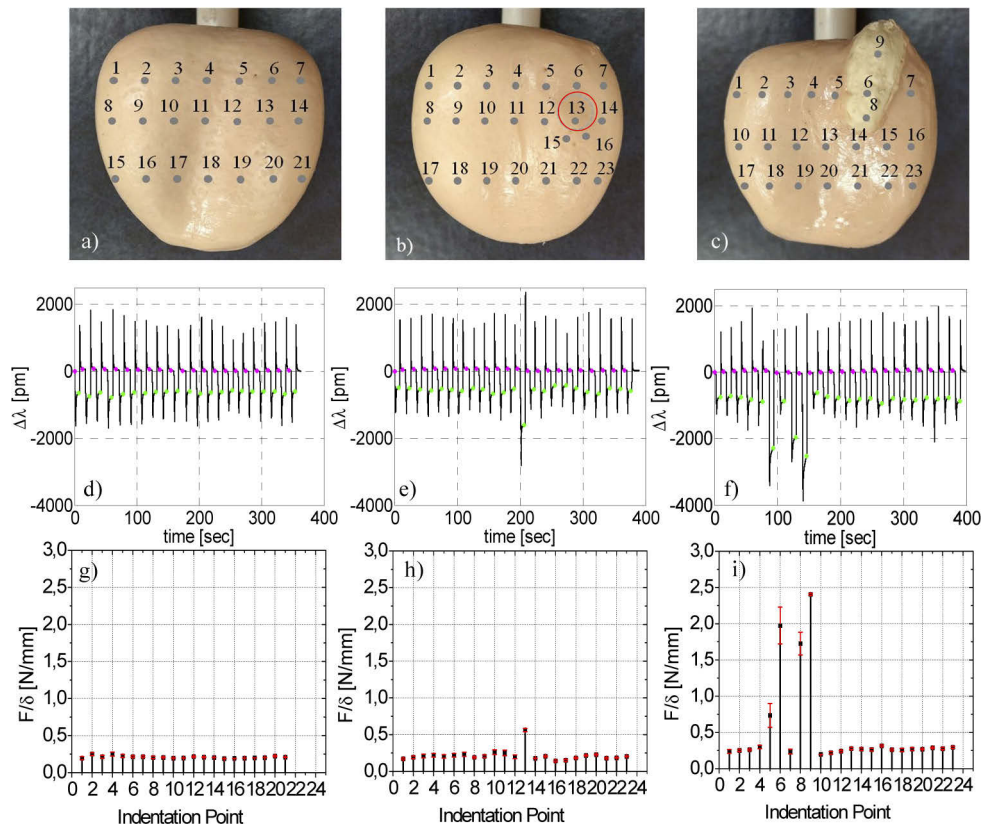
Fig. 5. Phantom prostate models selected for the experimental tests: benign prostate (a), early stage of carcinoma (b) and compact external mass on the surface (c) models. Wavelength shift as a function of time for benign model prostate (d), for the early stage of carcinoma (e) and for compact external mass on the surface (f) models. Ratio F/ δ as a function of time measured during the indentation test of benign model prostate (g), of the early stage of carcinoma (h) and compact external mass on the surface (i) models.

for prostate 3, where three points (#6, 8 and 9) exhibit values (1.97 N/mm, 1.72 N/mm, and 2.40 N/mm respectively) well above the average (that is 0.285 N/mm). Overall, these results demonstrate that our sensor is able to discriminate between healthy and diseased zones of the gland.

3.3. *Tests ex vivo*

In order to validate the developed probe in conditions very close to the final realistic scenario, indentation experiments on real prostates obtained from radical surgeries of patients were also performed (see Fig. 6). In particular, two prostates were here analyzed. The first one is a healthy prostate obtained by a cystectomy surgery on a patient with a bladder cancer, while the second one is a diseased prostate (Gleason score 8 according to the biopsy analysis performed before the surgery) obtained by a radical prostatectomy surgery. In fact, Gleason score is a histological grade of the single lesion and is positively correlated with the prostate local stiffness. [36]

    The two prostates were indented 4 times along the above mentioned lines (apex, midgland and base) corresponding to a total of 12 points. The indentation depth was fixed to 2 millimeters for all the points. The measured sensorgrams are shown in Fig. 7(a) and Fig. 7(b) for the healthy and diseased prostate, respectively. The force values were then obtained starting from the Bragg
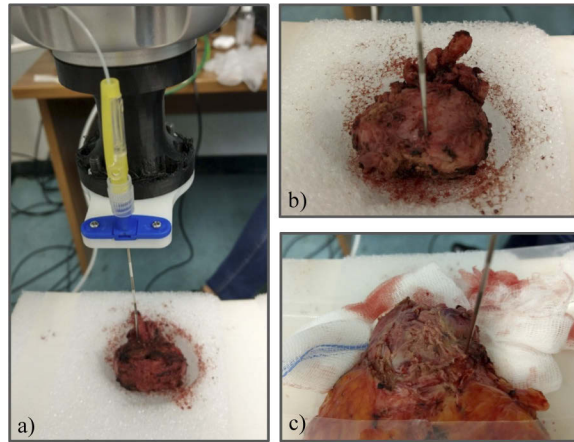
Fig. 6. Optical probe installed on a robotic arm during the *ex vivo* test of the diseased (a,b) and healthy (c) prostate.

wavelength shifts evaluated as the difference between the point corresponding to f_{dz}=0,05N (magenta point) and the minimum value (red point).
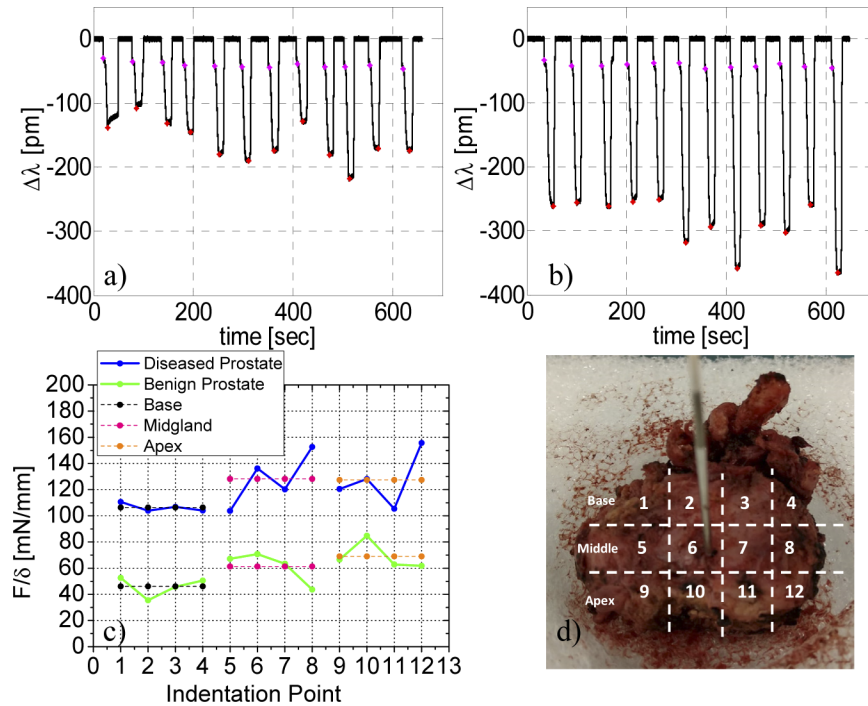

Fig. 7. Sensorgrams returned by the optical probe during the healthy (a) and diseased (b) prostate organs. (c) Ratio F/δ for *ex vivo* indentation of healthy and diseased organs in the 12 points mapped as (d)

The *F/δ* values pertaining to the healthy gland are shown as green line in Fig. 7(c) The average values of the base, midgland and apex zone are 46 mN/mm, 61 mN/mm and 69 mN/mm, respectively. It is worth noting that the increasing trend of the force as a function of the time is

due to the fact that the indentation points move from the softer area of the prostate (i.e. the base, up to a harder zone, i.e. the apex). In particular, the first 4 points are relative to the base that is generally softer than the rest of the organ [37,38]. Moreover, the force values in the middle and base regions exhibit an oscillating trend and a comparable average value. This means that an eventual dehydration phenomenon is not so significant, also in view of the fact that the duration of the whole experiment is only 12 minutes.

The data pertaining to the diseased prostate are shown in Fig. 7(c) as a blue line. In this case, the F/δ values are significantly higher over the whole surface. This result is coherent with the biopsy, that confirms a diffused tumor over the whole gland. Specifically, the average value of the base, midgland and apex zone are 106 mN/mm, 128 mN/mm and 127 mN/mm, respectively. Overall, the average F/δ of the diseased prostate (120 mN/mm) is about 2 times larger than that pertaining to the healthy one (59 mN/mm).

Finally, we tried to compare the achieved results with those reported in the previous works. Indeed, the results pertaining to previous prostate indentation experiments are presented in terms of Young modulus. The Young modulus E can be derived from Eq. (1), considering the case of a cylindrical flat tip indentation [39] with $n=1$ and $g=2R_f$ (R_f=0,45mm is the probe radius):

$$E = \frac{F \cdot (1 - \nu^2)}{2 \cdot R_f \cdot \delta}. \tag{2}$$

As mentioned before, this expression is valid only if the prostate is perfectly elastic and the rigidity of our indenter is several order of magnitude larger than that of the biological tissue. By substituting the values in the above equation (ν=0.5 in our case) we find that the average value of E for the healthy and diseased prostates are 50 kPa ($\pm$11 kPa) and 101 kPa ($\pm$15 kPa) respectively. These results are consistent with those previously obtained in indentation experiments [1], although there is a marked variability in the results depending on testing techniques and disease state of the prostate tissue. The resolution in measuring the elastic modulus can be derived from Eq. (2) by considering that the resolution in measuring the force F is 1mN. However, the relationship between E and F depends on the indentation depth δ. In other words, we obtain different resolutions for elastic module as a function of the indentation depth. Larger indentation depths give rise to best (smaller) resolution, and specifically 0.86, 0.43 and 0.28 kPa for indentation depths of 1, 2 and 3 mm respectively. It is important to underline that the evaluation of the elastic modulus of biological tissues is not trivial, and the estimated values strongly depends on the technique used to determine it [40]. However, in a clinical scenario, we envision the use of the ratio between the force and the indentation depth as reliable indicator to discriminate between healthy and diseased areas of the prostate. Actually, the above mentioned ratio contains all the measured data that would be used to calculate the Young Modulus. In this respect, our preliminary results sound promising.

So far, only preliminary tests were performed, and further experiments are necessary to assess the validity of our technique for the clinical practice. Although the results achieved so far look very promising, a larger number of indentation points is strictly necessary to mitigate the risk that the mechanical heterogeneity within the prostate could result in misleading measurement.

Our system is intended to be used only with a robotic arm since it is necessary to have a stable control on the indentation depth, avoiding manual vibrations that would cause significant measurements errors. Indeed, a non-perpendicular contact between the probe and the tissue would affect the measure of the stiffness, due to the presence of a shear component to the force relative to the sensor. In order to make the probe less sensitive to indentation angle, the optical fiber tip can be suitably modified to create microspheres by means of low cost approaches [41]. Eventually, an additional six-axis force-torque sensor could be mounted at the end-effector of the manipulator; by measuring the torque generated during the measurement in case of a

non-orthogonal contact, a zero-torque control would bring the probe orthogonal to the surface undergoing the inspection.

At this stage, the developed probe does not provide information about the surface texture of the prostate, although this parameter is inherently subjective. However, information about the surface roughness could be in principle derived from the analysis of the sensorgram (*cfr.* Figure 7(a) and (b)), and in particular by analyzing the optical signal in the time windows in which the admittance control takes place. In fact, the admittance control was developed just to circumvent the problem related to the surface non-uniformity, with the aim to determine the contact point between the probe and the prostate. Indeed, strong differences in the optical signal between adjacent points at the admittance control times stand for different contact points indicating high non-uniformity.

Finally, it is worth noting that the biological changes which determine the increase of the prostate stiffness (increase in cellular density and collagen content) occur from the early stage of the tumor development [9,42]. Associations between increasing cancer stage and increasing stiffness have also been extensively reported [43]. In this respect, our sensor allows to analyze a very small section of the prostate (*i.e.* an area of about 0.6 mm^2), thus opening the way to novel diagnostic tools for early stage cancer detection.

4. Conclusions

In this work, we have presented an optical fiber probe for mechanical characterization of prostatic tissue. The optical probe is made of a customized FBG used to measure the force acting on its tip during the indentation of specific tissue points with a sensitivity of about 1 nm/Newton. The probe is suitably integrated on a robotic arm that allows achieving a fully controlled movement. The developed probe was first validated on both silicone membranes and phantom tissues mimicking different stages of the prostatic carcinoma. Successively, *ex vivo* tests on real prostates obtained from patients were carried out. Preliminarily results demonstrate that our system is able to discriminate between healthy and diseased prostatic glands. Further experiments are needed to assess the capability of our device to distinguish among different Gleason score level of carcinoma. Overall, our results lay the foundation for the development of an optical fiber probe to be directly integrated into biopsy needles to perform *in vivo* mechanical measurements of the prostatic tissue. Our device should not be seen as alternative but instead complementary to the traditional techniques currently used for prostate cancer screening. In particular, our system could become a powerful tool to guide and improve the transrectal biopsy technique through the expression of mechanical characteristics of the tissue, otherwise not obtainable during biopsy. The small dimensions (probe diameter of 0,9mm) may allow achieving unprecedented levels of spatial resolution making possible, in principle, to identify sub millimeter sized prostatic carcinoma arising at the early stages.

Disclosures. The authors declare no conflict of interest.

Data availability. The Ethics Committee of the University of Naples "Federico II" approved the experiments. Informed consent was obtained from all subjects.

References

1. N. P. Kelly, H. D. Flood, D. A. Hoey, P. A. Kiely, S. K. Giri, J. C. Coffey, and M. T. Walsh, "Direct mechanical characterization of prostate tissue—a systematic review," Prostate **79**(2), 115–125 (2019).
2. D. W. Good, G. D. Stewart, S. Hammer, P. Scanlan, W. Shu, S. Phipps, R. Reuben, and A. S. McNeill, "Elasticity as a biomarker for prostate cancer: a systematic review," BJU Int. **113**(4), 523–534 (2014).

3. A. L. Walsh, S. W. Considine, A. Z. Thomas, T. H. Lynch, and R. P. Manecksha, "Digital rectal examination in primary care is important for earlydetection of prostate cancer: a retrospective cohort analysis study," Br J Gen Pract **64**(629), e783–e787 (2014).

4. A. Hoogendam, F. Buntinx, and H. C. de Vet, "The diagnostic value of digital rectal examination in primary care screening for prostate cancer: ameta-analysis," Fam Pract. **16**(6), 621–626 (1999).

5. P. Qin, K. Wu, Y. Hu, J. Zeng, and X. Chai, "Diagnosis of benign and malignant thyroid nodules using combined conventional ultrasound and ultrasound elasticity imaging," IEEE J. Biomed. Health Inform. **24**(4), 1028–1036 (2020).

6. C. H. Liu, Y. Du, M. Singh, C. Wu, Z. Han, J. Li, A. Chang, C. Mohan, and K. V. Larin, "Classifying murine glomerulonephritis using optical coherence tomography and optical coherence elastography," J. Biophotonics **9**(8), 781–791 (2016).

7. J. Q. Liu, W. J. Chen, M. J. Zhou, W. F. Li, and J. Tang, "Ultrasound-based multimodal imaging predicting ischemic-type biliary lesions after living-donor liver transplantation," IJGM **14**, 1599–1609 (2021).

8. B. Ahn, E. I. S. Lorenzo, K. H. Rha, H. J. Kim, and J. Kim, "Robotic palpation-based mechanical property mapping for diagnosis of prostate cancer," Journal of Endourology **25**(5), 851–857 (2011).

9. W. C. Carson, G. J. Gerling, T. L. Krupski, C. G. Kowalik, J. C. Harper, and C. A. Moskaluk, "Material characterization of ex vivo prostate tissue via spherical indentation in the clinic," Medical Engineering & Physics **33**(3), 302–309 (2011).

10. S. Phipps, T. H. J. Yang, F. K. Habib, R. L. Reuben, and S. A. Mcneill, "Measurement of the mechanical characteristics of benign prostatic tissue: a novel method for assessing benign prostatic disease," Urology **65**(5), 1024–1028 (2005).

11. S. Zein, F. T. Ghomsheh, and H. Jamshidian, "Evaluation of artificial tactile sense in mass detection in silicone phantom for the diagnosis of prostate tumor," Bull. Exp. Biol. Med. **169**(4), 497–503 (2020).

12. Q. Peng, S. Omata, D. M. Peehl, and C. E. Constantinou, "Stiffness mapping prostate biopsy samples using a tactile sensor," *Annual. Int Conf IEEE Eng Med Biol Soc.* (2011).

13. M. Jia, J. W. Zu, and A. Hariri, "A new tissue resonator indenter device and reliability study," Sensors **11**(1), 1212–1228 (2011).

14. V. Jalkanen, "Hand-held resonance sensor for tissue stiffness measurements—a theoretical and experimental analysis," Meas. Sci. Technol. **21**(5), 055801 (2010).

15. V. Mishra, N. Singh, U. Tiwari, and P. Kapur, "Fiber grating sensors in medicine: current and emerging applications," Sens. Actuators, A **167**(2), 279–290 (2011).

16. P. Roriz, L. Carvalho, O. Frazão, J. L. Santos, and J. A. Simões, "From conventional sensors to fibre optic sensors for strain and force measurements in biomechanics applications: A review," Journal of Biomechanics **47**(6), 1251–1261 (2014).

17. P. Roriz, O. Frazão, A. B. Lobo-Ribeiro, J. L. Santos, and J. A. Simões, "Review of fiber-optic pressure sensors for biomedical and biomechanical applications," J. Biomed. Opt **18**(5), 050903 (2013).

18. J. Liab, S. J. Hammerc, W. M. Shud, R. R. J. Maiera, D. P. Handa, R. L. Reubenc, and W. N. MacPhersona, "An optical fibre dynamic instrumented palpation sensor for the characterisation of biological tissue," Sens. Actuators, A **225**, 53–60 (2015).

19. S. V. Beekmans and D. Iannuzzi, "Characterizing tissue stiffness at the tip of a rigid needle using an opto-mechanical force sensor," Biomed Microdevices **18**(1), 15 (2016).

20. C. Lv, S. Wang, and C. Shi, "A high-precision and miniature fiber bragg grating-based force sensor for tissue palpation during minimally invasive surgery," Ann. Biomed. Eng. **48**(2), 669–681 (2020).

21. K. S. Shahzadaa, A. Yurkewicha, R. Xua, and R. V. Patela, "Sensorization of a surgical robotic instrument for force sensing," Proc. of SPIE **9702**, 97020U (2016).

22. T. Li, C. Shi, and H. Ren, "A high-sensitivity tactile sensor array based on Fiber Bragg grating sensing for tissue palpation in minimally invasive surgery," IEEE/ASME Trans. Mechatron. **23**(5), 2306–2315 (2018).

23. H. Liu, J. Li, X. Song, L. D. Seneviratne, and K. Althoefer, "Rolling indentation probe for tissue abnormality identification during minimally invasive surgery," IEEE Trans. Robot. **27**(3), 450–460 (2011).

24. B. Hartmann, G. Marchi, P. Alberton, Z. Farkas, A. Aszodi, J. Roths, and H. C. Schaumann, "Early detection of cartilage degeneration: a comparison of histology, Fiber Bragg grating-based micro-indentation, and atomic force microscopy-based nano-indentation," IJMS **21**(19), 7384 (2020).

25. B. Carotenuto, A. Micco, A. Ricciardi, E. Amorizzo, M. Mercieri, A. Cutolo, and A. Cusano, "Optical guidance systems for epidural space identification," IEEE J. Sel. Top. Quantum Electron. **23**(2), 371–379 (2017).

26. B. Carotenuto, A. Ricciardi, A. Micco, E. Amorizzo, M. Mercieri, A. Cutolo, and A. Cusano, "Optical fiber technology enables smart needles for epidurals: an in-vivo swine study," Biomed. Opt. Express **10**(3), 1351–1364 (2019).

27. B. Carotenuto, A. Ricciardi, A. Micc, E. Amorizzo, M. Mercieri, A. Cutolo, and A. Cusano, "Smart optical catheters for epidurals," Sensors **18**(7), 2101 (2018).

28. https://fbgs.com/components/draw-tower-gratings-dtgs/

29. K. O. Hill and G. Meltz, "Fiber Bragg grating technology fundamentals and overview," J. Lightwave Technol. **15**(8), 1263–1276 (1997).

30. https://lunainc.com/product/si155-optical-sensing-instrument

31. A. Cirillo, F. Ficuciello, C. Natale, P. Pirozzi, and L. Villani, "A conformable force/tactile skin for physical human–robot interaction," IEEE Robot. Autom. Lett. **1**(1), 41–48 (2016).

32. H. Z. Lan and T. A. Venkatesh, "On the relationships between hardness and the elasticand plastic properties of isotropic power-law hardening materials," Philos. Mag. **94**(1), 35–55 (2014).

33. K. Larson, "Can you estimate modulus from durometer hardness for silicones? Yes, but only roughly . . . and you must choose your modulus carefully," (2019), https://www.dow.com/content/dam/dcc/documents/en-us/tech-art/11/11-37/11-3716-01-durometer-hardness-for-silicones.pdf?iframe=true

34. B. J. Briscoe, K. S. Sebastian, and M. J. Adams, "The effects of indenter geometry on the elastic response to indentation," J. Phys. D: Appl. Phys. **27**(6), 1156–1162 (1994).

35. B. Bhushan, "Depth sensing nanoindentation measurement techniques and applications," Microsyst. Technol. **23**(5), 1595–1649 (2017).

36. Y. Ji, L. Ruan, W. Ren, G. Dun, J. Liu, Y. Zhang, and Q. Wan, "Stiffness of prostate gland measured by transrectal real-time shear wave elastography for detection of prostate cancer: a feasibility study," BJR **92**(1097), 20180970 (2019).

37. B. M. Ahn, J. Kim, L. Ian, K. H. Rha, and H. J. Kim, "Mechanical property characterization of prostate cancer using a minimally motorized indenter in an ex vivo indentation experiment," Urology **76**(4), 1007–1011 (2010).

38. A. Goddi, A. Sacchi, G. Magistretti, and J. Almolla, "Transrectal real-time elastography of the prostate: normal patterns," J. Ultrasound **14**(4), 220–232 (2011).

39. A. C. Chang and B. H. Liu, "Modified flat-punch model for hyperelastic polymeric and biological materials in nanoindentation," Mech. Mater. **118**, 17–21 (2018).

40. C. T. McKee, J. A. Last, P. Russell, and C. I. Murphy, "Indentation versus tensile measurements of Young's modulus for soft biological tissues," Tissue Eng Part B Rev. **17**(3), 155–164 (2011).

41. H. Yu, Q. Huang, and J. Zhao, "Fabrication of an optical fiber micro-sphere with a diameter of several tens of micrometers," Materials **7**(7), 4878–4895 (2014).

42. S. A. Tomlins, R. Mehra, D. R. Rhodes, X. Cao, L. Wang, S. M. Dhanasekaran, S. Kalyana-Sundaram, J. T. Wei, M. A. Rubin, K. J. Pienta, R. B. Shah, and A. M. Chinnaiyan, "Integrative molecular concept modeling of prostate cancer progression," Nat Genet **39**(1), 41–51 (2007).

43. K. Hoyt, B. Castaneda, M. Zhang M, P. Nigwekar, P. A. di Sant'agnese, J. V. Joseph, J. Strang, D. J. Rubens, and K. J. Parker, "Tissue elasticity properties as biomarkers for prostate cancer," CBM **4**(4-5), 213–225 (2008).